Lagrangian Coherent Structures

George Haller

Institute of Mechanical Systems, ETH Zürich, 8092 Zürich, Switzerland;
email: georgehaller@ethz.ch

Keywords

mixing, turbulence, transport, invariant manifolds, nonlinear dynamics

Abstract

Typical fluid particle trajectories are sensitive to changes in their initial conditions. This makes the assessment of flow models and observations from individual tracer samples unreliable. Behind complex and sensitive tracer patterns, however, there exists a robust skeleton of material surfaces, Lagrangian coherent structures (LCSs), shaping those patterns. Free from the uncertainties of single trajectories, LCSs frame, quantify, and even forecast key aspects of material transport. Several diagnostic quantities have been proposed to visualize LCSs. More recent mathematical approaches identify LCSs precisely through their impact on fluid deformation. This review focuses on the latter developments, illustrating their applications to geophysical fluid dynamics.

1. INTRODUCTION

Material coherence emerges ubiquitously in fluid flows around us (**Figure 1**). It admits distinct signatures in virtually any diagnostic scalar field or reduced-order model associated with these flows. Signatures, however, do not reveal the root cause of flow coherence. The theory of Lagrangian coherent structures (LCSs) seeks to isolate this root cause by uncovering special surfaces of fluid trajectories that organize the rest of the flow into ordered patterns.

Lagrangian fluid motion is inherently unstable owing to its sensitivity with respect to initial conditions. Velocity model comparisons based on advecting individual fluid particles are therefore virtually guaranteed to produce poor results. By contrast, LCSs are robust features of Lagrangian fluid motion that point beyond idiosyncrasies of individual trajectories and enable a systematic comparison of models with experiments and with each other.

The LCS acronym was coined by Haller & Yuan (2000) to describe the most repelling, attracting, and shearing material surfaces that form the skeletons of Lagrangian particle dynamics. Uncovering such surfaces from experimental and numerical flow data promises a simplified understanding of the overall flow geometry, an exact quantification of material transport, and a powerful opportunity to forecast, or even influence, large-scale flow features and mixing events.
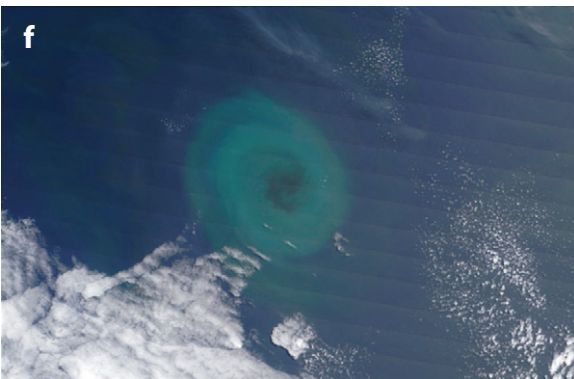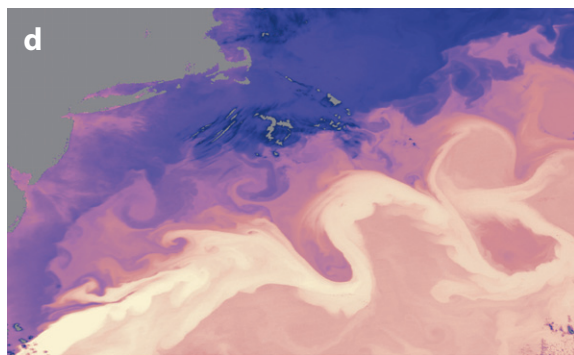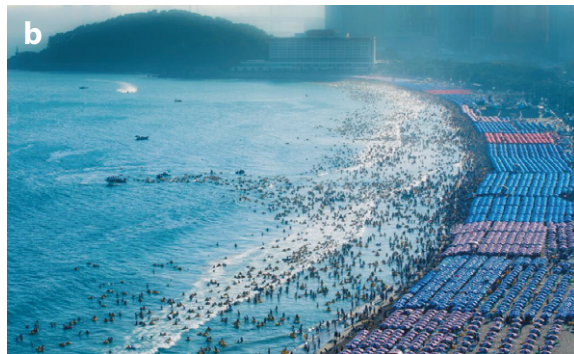
Classic dynamical systems theory offers major help in analyzing Lagrangian coherence in autonomous (i.e., time-independent), time-periodic, and quasiperiodic velocity fields. It reveals a wealth of recurrent motions in such temporally idealized flows, ranging from simple fixed points through periodic orbits to stable and unstable manifolds, KAM (Kolmogorov-Arnold-Moser) tori, and chaotic invariant sets (Guckenheimer & Holmes 1983). In the limit of infinitely long times, these recurrent structures gain decisive influence over tracer patterns and become the LCSs of the flow (**Figure 2**).

This situation changes drastically for temporally aperiodic flows, such as those in **Figure 1**. These flows have no fixed points or stable and unstable manifolds tied to fixed points. No fluid particle in the ocean or atmosphere will form a periodic orbit or a KAM torus either. Thus, although the comparisons made in **Figure 2** with the observed patterns of **Figure 1** are truly inspiring, one needs to remember that the idealized trajectories shown in **Figure 2** simply do not exist in realistic fluid flows.

Three basic approaches aim to close the gap between real-life observations and classic nonlinear flow structures. First, one may identify the idealized structures of **Figure 2** in a temporally simplified (steady, time-periodic, or quasiperiodic) analytic model and conjecture the existence of similar structures in the true flow by analogy. Several accessible reviews discuss this approach (see Ottino 1989; Wiggins 1992, 2005; Jones & Winkler 2002; Samelson & Wiggins 2006). Second, one may run heuristic flow diagnostics on temporally complex flow data and point out similarities between features of the diagnostics and observed flow patterns. Comprehensive reviews of this

Figure 1

Coherent Lagrangian patterns in nature. (*a*) Spiral eddies in the Mediterranean Sea in 1984 (Paul Scully-Power/NASA). (*b*) Swimmers carried by a rip current at Haeundae Beach, South Korea, in the summer of 2012. Panel *b* courtesy of Joo Yong Lee/Sungkyunkwan University. (*c*) A sudden extension of the Deepwater Horizon oil spill in the Gulf of Mexico in June 2010 (NASA). (*d*) Transport of warm water revealed by the sea surface temperature distribution around the Gulf Stream in 2005 (NASA). (*e*) Jupiter's Great Red Spot seen from the Voyager 1 mission in February 1979 (NASA/JPL, with image processing by Björn Jónsson). (*f*) Phytoplankton bloom east of Tasmania (Jeff Schmaltz/MODIS Rapid Response Team, NASA/GSFC). (*g*) Water carried by a tornado off the Florida Keys (Joseph Golden/NOAA). (*h*) Steam rings blown by Mount Etna in November 2013. Panel *h* courtesy of Tom Pfeiffer/**http://www.volcanodiscovery.com**.

Saddle fixed point
Compare with Figure 1*b,c*

Center fixed point
Compare with Figure 1*e,f*

Homoclinic tangle
Compare with Figure 1*a*

Steady shear flow
Compare with Figure 1*d*

Steady shear flow
Compare with Figure 1*g*

KAM torus
Compare with Figure 1*h*

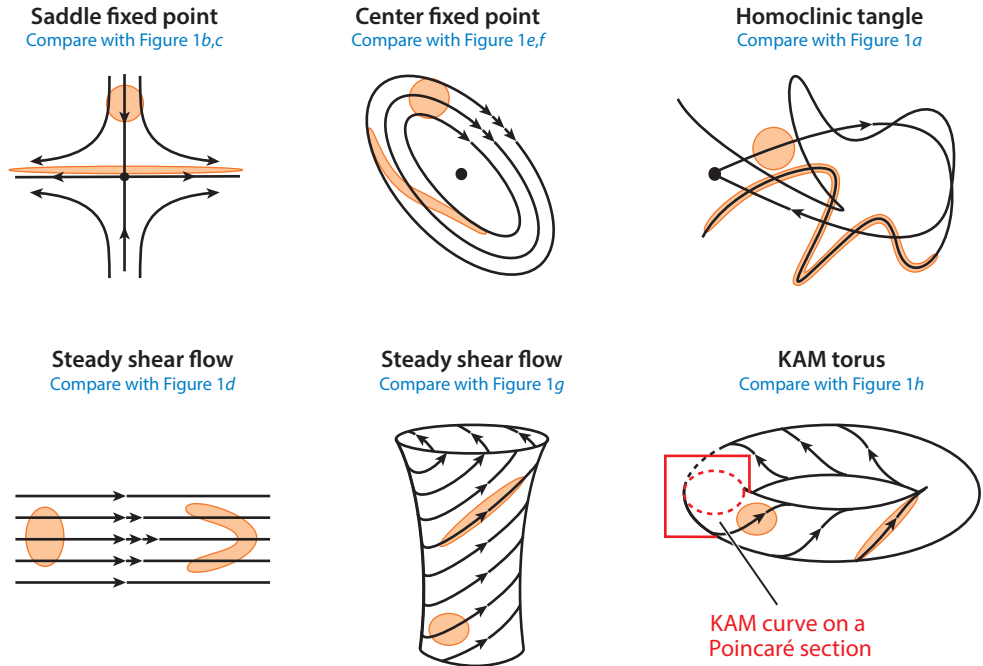KAM curve on a
Poincaré section

Figure 2

Classic dynamical system structures in steady and time-periodic fluid flows that are reminiscent of the flow patterns in **Figure 1**. Abbreviation: KAM, Kolmogorov-Arnold-Moser.

approach are given by Provenzale (1999), Boffetta et al. (2001), Jones & Winkler (2002), Peacock & Dabiri (2010), and Samelson (2013).

The present review surveys a third approach. Instead of cataloging idealized motions and then pointing out their impact on tracers as a side result (**Figure 2**), I focus on deconstructing observed types of material coherence, such as those in **Figure 1**, and then seek the exact dynamical structures that create these forms of coherence in nonidealized flow data.

This inverse problem necessitates a careful rethinking of nonlinear dynamical systems theory for finite-time flows, ultimately revealing previously unknown, yet all-pervasive LCSs. I review the principles and mathematics underlying this approach below and show how it brings a new level of understanding to complex geophysical flow data.

Further mathematical methods outside the scope of this review target the interiors of coherent flow regions, as opposed to the LCSs bounding these regions. Examples include probabilistic methods for detecting almost-invariant and finite-time coherent sets (Froyland & Padberg-Gehle 2014), ergodicity-based methods for time-periodic flows (Budišić & Mezić 2012), and braid-theoretical methods for flows with recurrent trajectories (Allshouse & Thiffeault 2012).

I also omit a survey of Eulerian diagnostic approaches to flow coherence, such as the Okubo-Weiss criterion (Okubo 1970, Weiss 1991), the Q-criterion (Hunt et al. 1988), the Δ-criterion (Chong et al. 1990), the Hua-Klein criterion (Hua & Klein 1998, Hua et al. 1998), and the λ_2-criterion (Jeong & Hussain 1995). These approaches can effectively frame coherent features of the instantaneous velocity field but lack objectivity (see Section 2.1). Furthermore, coherently evolving velocity features tend to differ substantially from coherently moving fluid parcels, and hence from LCSs, in unsteady flows (see, e.g., Beron-Vera et al. 2013).

2. REQUIREMENTS FOR A SELF-CONSISTENT LAGRANGIAN COHERENT STRUCTURE THEORY

I start with a set of basic requirements that have proven necessary for self-consistent LCS results on benchmark problems.

2.1. Objectivity

A fundamental axiom of mechanics is objectivity, which postulates that material response is independent of the observer (Gurtin 1981). Objectivity requires that we add Coriolis and centrifugal forces to the Navier-Stokes equations in a rotating frame so that the velocity field solving these equations in the rotating frame generates the same material evolution as in an inertial frame.

LCSs, as skeletons of material response, should therefore be objectively identified. An LCS theory is objective if its conclusions are invariant under Euclidean coordinate changes of the form

$$y = Q(t)x + p(t), \tag{1}$$

with $Q(t)$ denoting a time-dependent proper orthogonal tensor and $p(t)$ denoting a time-dependent translation (Truesdell & Noll 2004).

Figure 3a illustrates the issue with nonobjective coherent structure detection. Most nonobjective diagnostics misclassify the unsteady flow shown, owing to its closed and rotating streamlines, as elliptic or vortical (Haller 2005). In reality, it is a rotating saddle flow, as shown by the evolving red tracer pattern initially seeded inside a closed streamline. Similar examples of hidden Lagrangian instabilities disguised by closed streamlines emerge from simulations of two-dimensional turbulence (see Section 5.1).

Instantaneous Eulerian diagnostics used in assessing Lagrangian coherence fail the test of objectivity (Haller 2005, Ouellette 2012). Objective Lagrangian diagnostics include relative and absolute dispersion (Provenzale 1999, Bowman 2000, Jones & Winkler 2002), finite-time Lyapunov exponents (FTLEs; see Section 4), finite-size Lyapunov exponents (FSLEs; see Aurell et al. 1997, Joseph & Legras 2002, d'Ovidio et al. 2004), effective diffusivity (Nakamura 1996, Haynes & Shuckburgh 2000, Shuckburgh & Haynes 2003), stretching in particle-fixed frames (Tabor & Klapper 1994, Lapeyre et al. 1999, Haller & Iacono 2003), affine versus nonaffine decomposition of material deformation (Kelley & Ouellette 2011), and invariants of the Cauchy-Green strain tensor (see Sections 5 and 6).

Early mathematical criteria for LCSs were all nonobjective sufficient conditions (Haller & Poje 1998; Haller 2000, 2001a, 2002). They assumed sustained saddle-type behavior in the Eulerian frame and gave bounds on the unsteadiness of the velocity field under which attracting and repelling surfaces also exist in the Lagrangian frame. As rigorous sufficient conditions, these results give no false positives for LCSs but may give false negatives in the selected frame. Later criteria for LCS based on the strain acceleration tensor (Haller 2001b, 2005; Duc & Siegmund 2008) were objective but still only sufficient, not necessary. Thus, these results may also give false negatives, albeit consistently in all frames.

Heuristic nonobjective LCS diagnostics (see, e.g., Mancho et al. 2013) are often simple to compute but may yield both false positives and false negatives in a given frame. This causes no harm in simple canonical examples, such as steady or time-periodic flows, for which one readily recognizes and discounts misclassified flow regimes (see, e.g., Mezić et al. 2010). Nonobjectivity, however, becomes a limitation in now-casting, transport estimating, and decision making in real time for complex flows, for which the correct answer is not a priori known.

2.2. Finite Time

The observed geophysical flow patterns of **Figure 1** evolve aperiodically during their finite life span. For such finite times, routinely used asymptotic concepts, such as stability, stable and unstable manifolds, and chaotic advection, become mathematically undefined. A Lagrangian method can only capture nonrecurrent material patterns systematically if it is designed for finite-time dynamical systems.

Most classic definitions of material stability, however, lose their ability to distinguish individual trajectories over finite times owing to the continuity of fluid trajectories with respect to initial positions. For instance, defining exceptional, hyperbolic fluid trajectories as those with nonzero FTLEs (Shadden et al. 2005, Wiggins 2005) would mark all but finitely many trajectories exceptional in any finite-time flow. Similarly, defining distinguished hyperbolic trajectories (DHTs) through a finite-time version of classic exponential dichotomies (Ide et al. 2002, Branicki & Wiggins 2009) would identify all fluid trajectories as DHTs in any finite-time flow. Mathematical approaches utilizing these ideas necessarily turn out to be problematic under scrutiny.

Even in recurrent infinite-time dynamical systems, finite-time tracer evolution is governed by LCSs different from those identified for asymptotic tracer motion. For instance, **Figure 3b** shows how an evolving attracting LCS provides the true finite-time centerpiece of a tracer pattern near a nonlinear saddle, as opposed to the classic unstable manifold of the saddle (Farazmand & Haller 2013).

2.3. Lagrangian Invariance

The word Lagrangian in the LCS acronym conveys that the detected material surface must be evolving with the flow. Several diagnostic approaches advertised as Lagrangian do not actually satisfy this requirement. Instead, they assess Lagrangian coherence over sliding time windows of the form $[t_0, t_0 + T]$, where the initial time t_0 sweeps through the observational time period.

Although this approach illustrates some aspects of flow evolution, the structures obtained at different t_0 values belong to different finite-time dynamical systems and generally do not evolve into each other. Sliding-window analysis is nevertheless widespread in the use of FTLEs, inspired by the expectation that ridges of these fields are almost invariant under variations of t_0 (see Section 4).

Figure 3c illustrates the issue with sliding-window-type approaches. In this steady flow example, sliding-window FTLE analysis gives a fixed ridge at $x = 0$ for all t_0 values, incorrectly suggesting a repelling LCS fixed along the y axis. The actual LCS is the black material line moving to the right, prevailing as the strongest repeller within an initially tightly stacked set of blue material lines (Haller 2011).
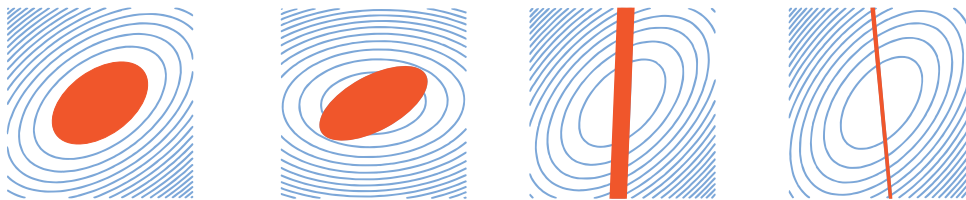
This example also underlines that LCSs are invariant surfaces in the extended phase space of position and time (see **Figure 4a**). In the space of positions, therefore, they move with the flow, even in steady flows. LCSs converge to classic invariant manifolds over longer times, should such manifolds exist in the infinite-time limit (**Figure 3b**).
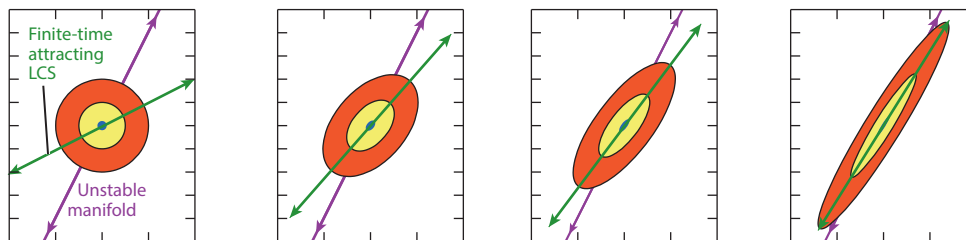
2.4. Spatial Convergence

Temporal convergence for a Lagrangian diagnostic field is meaningless in a finite-time setting, but spatial convergence to a continuous limit is reasonable to expect under computational grid refinement. This is to ensure that the field uniquely identifies a material point as part of an LCS.

Virtually all Lagrangian approaches are associated with the flow map, which advects all fluid particles over the same time interval, thereby mimicking experimental flow visualization by tracers.
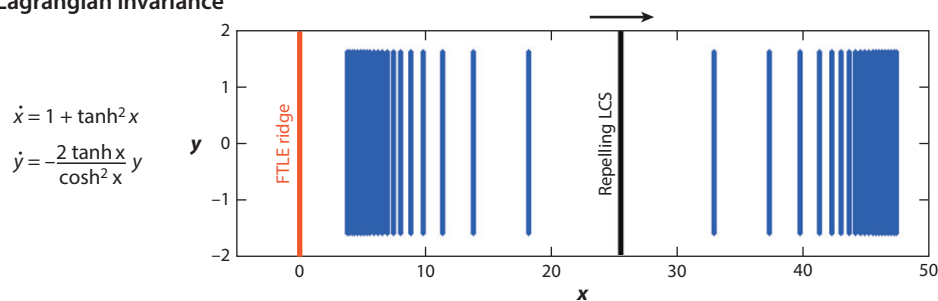
a Objectivity

b Finite-time nature

Finite-time attracting LCS

Unstable manifold

c Lagrangian invariance

$$\dot{x} = 1 + \tanh^2 x$$

$$\dot{y} = -\frac{2\tanh x}{\cosh^2 x}\, y$$

FTLE ridge

Repelling LCS

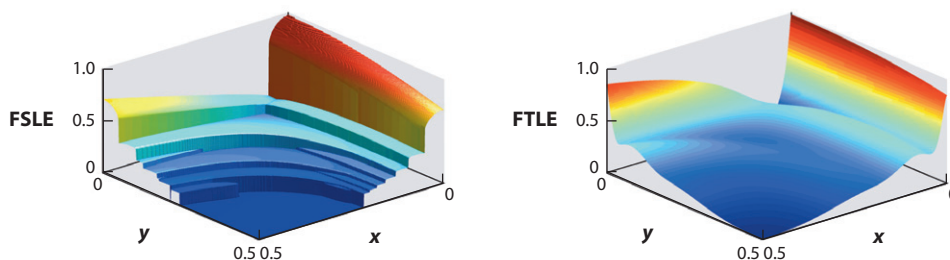### d Spatial convergence

FSLE

FTLE

Figure 3

Basic Lagrangian coherent structure (LCS) benchmarks. (*a*) A rotating saddle misclassified as a vortex by most nonobjective diagnostics. Panel *a* courtesy of Francisco J. Beron-Vera. (*b*) Finite-time attracting LCS (*green*) not captured by the classic unstable manifold (*purple*) near a nonlinear saddle point. Panel *b* adapted with permission from Farazmand & Haller (2013). (*c*) Lack of Lagrangian invariance in sliding-window finite-time Lyapunov exponent (FTLE) analysis. Panel *c* adapted with permission from Haller (2011). (*d*) A discontinuous finite-size Lyapunov exponent (FSLE) field and smooth FTLE field over the same grid for a steady gyre. Panel *d* adapted with permission from Karrasch & Haller (2013).
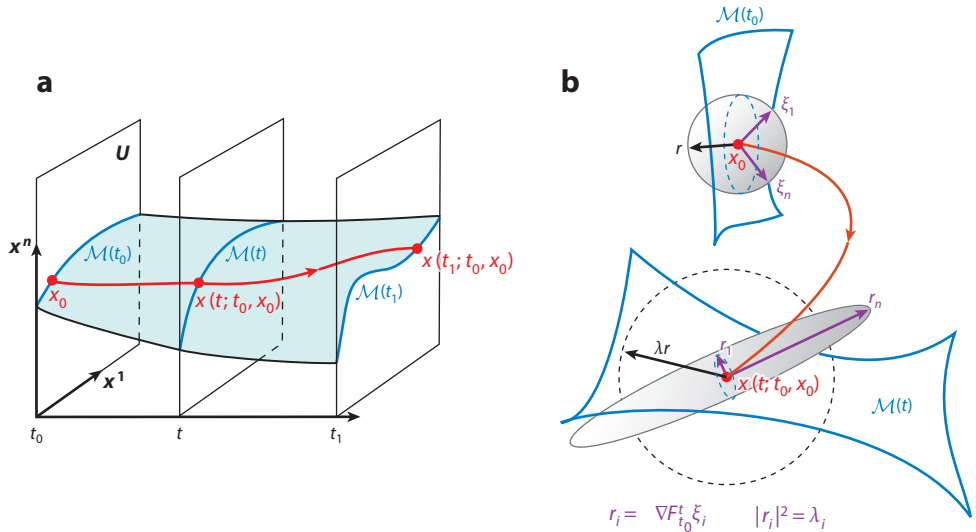
Figure 4

(*a*) Material surface evolution in the extended phase space. (*b*) Material surface evolution in the phase space, the geometry of the invariants of the Cauchy-Green strain tensor C, and their relation to the generalized Green-Lagrange deformation tensor E_λ.

For a smooth (or smoothed) velocity data set, the flow map is a smooth function of initial conditions over finite times (Arnold 1973); thus spatial convergence is not an issue.

A notable exception is FSLE analysis, which involves running the flow map over different times for different initial conditions, until local stretching reaches a prescribed threshold (Aurell et al. 1997, Lai & Tél 2011). This computation generically leads to intrinsic jump discontinuities in the FSLE field along codimension-one surfaces of initial conditions (Karrasch & Haller 2013). **Figure 3d** shows these FSLE discontinuities for a steady gyre flow, while the FTLE field remains smooth for the same grid resolution.

3. OBJECTIVE DESCRIPTION OF LAGRANGIAN DEFORMATION

Here I review the classic objective quantities describing material deformation and survey computational methods targeting these quantities in fluid flows. I start with a velocity field $v(x, t)$, which generates trajectories through the differential equation

$$\dot{x} = v(x, t), \qquad x \in U, \quad t \in [t_0, t_1]. \tag{2}$$

The positions $x = (x^1, x^2, x^3)$ vary in a bounded flow domain $U \subset \mathbb{R}^3$, with times t ranging over a finite time interval $[t_0, t_1]$. The solutions of Equation 2 are denoted by $x(t; t_0, x_0)$, with x_0 referring to the initial position at time t_0. In the case of two-dimensional flows, we have $x = (x^1, x^2)$ and $U \subset \mathbb{R}^2$ in Equation 2.

3.1. Flow Map

Central to the Lagrangian description of fluid motion is the flow map

$$F_{t_0}^t(x_0) := x(t; t_0, x_0), \qquad x \in U, \quad t \in [t_0, t_1], \tag{3}$$

taking an initial position x_0 to its current position $x(t; t_0, x_0)$ at time t. For any smooth velocity field $v(x, t)$, the flow gradient $\nabla F_{t_0}^t(x_0)$ is an invertible matrix, serving as the normalized fundamental matrix solution of the equation of variations (Arnold 1973)

$$\dot{y} = \nabla v(x(t; t_0, x_0))y. \tag{4}$$

Let us consider a hypersurface $\mathcal{M}(t_0)$ of initial fluid positions (i.e., a smooth set that has dimension one less than that of U). A material surface

$$\mathcal{M}(t) := F_{t_0}^t(\mathcal{M}(t_0)) \tag{5}$$

will then be the time-t position of the initial surface $\mathcal{M}(t_0)$ evolving under the flow (see **Figure 4a**).

3.2. Strain Tensors

In exploring Lagrangian coherence, we are interested in finding material surfaces $\mathcal{M}(t)$ with an exceptional impact on the deformation of nearby material elements. The local deformation along any trajectory traveling in $\mathcal{M}(t)$ is reflected by the evolution of infinitesimal perturbations $y(t)$ to the trajectory. These perturbations evolve under Equation 4 and can be written as $y(t) = \nabla F_{t_0}^t(x_0)y(t_0)$ because $\nabla F_{t_0}^t(x_0)$ is the fundamental matrix solution of Equation 4 satisfying $\nabla F_{t_0}^{t_0}(x_0) = I$. The squared magnitude of an evolving perturbation at the final time t_1 is therefore equal to

$$|y(t_1)|^2 = \langle \nabla F_{t_0}^{t_1}(x_0)y(t_0), \nabla F_{t_0}^{t_1}(x_0)y(t_0) \rangle = \langle y(t_0), C(x_0)y(t_0) \rangle,$$

where the right Cauchy-Green strain tensor $C(x_0)$ is defined as (Truesdell & Noll 2004)

$$C(x_0) = \left[\nabla F_{t_0}^{t_1}(x_0) \right]^T \nabla F_{t_0}^{t_1}(x_0). \tag{6}$$

This symmetric tensor is positive definite owing to the invertibility of $\nabla F_{t_0}^{t_1}$. The eigenvalues $\lambda_i(x_0)$ and eigenvectors $\xi_i(x_0)$ of $C(x_0)$ satisfy

$$C\xi_i = \lambda_i \xi_i, \quad |\xi_i| = 1, \quad i = 1, \dots, n; \quad 0 < \lambda_1 \leq \dots \leq \lambda_n, \quad \xi_i \perp \xi_j, \quad i \neq j, \tag{7}$$

where $n = 2$ for two-dimensional flows, and $n = 3$ for three-dimensional flows. The tensor C and its invariants depend on the choice of the time interval $[t_0, t_1]$, suppressed here for notational simplicity. In incompressible flows, $\det C = \prod_i \lambda_i \equiv 1$ holds. Thus, for generic x_0 locations, for which the eigenvalues of C are not repeated, we have

$$0 < \lambda_1 < 1 < \lambda_n.$$

Figure 4b illustrates the geometric meaning of the invariants of the Cauchy-Green deformation tensor. An infinitesimally small sphere initialized at point x_0 is carried by the flow along the trajectory $x(t; t_0, x_0)$ into a small ellipsoid, whose n principal axes are aligned with the vectors $r_i(x_0) = \nabla F_{t_0}^{t_1}(x_0)\xi_i(x_0)$. The length of the i-th principal axis is $\sqrt{\lambda_i(x_0)}$ times the radius of the initial sphere.

We also use a generalized family of Green-Lagrange strain tensors defined as

$$E_\lambda(x_0) = \frac{1}{2}[C(x_0) - \lambda^2 I], \quad \lambda > 0, \tag{8}$$

which measures the deviation of the infinitesimal deformation at x_0 from a uniform spherical expansion by a factor of λ, as illustrated in **Figure 4**. For $\lambda = 1$, we recover the classic Green-Lagrange tensor, as defined by Truesdell & Noll (2004). The tensor $E_\lambda(x_0)$ is symmetric but generally not positive definite. Indeed, its eigenvalues are $\nu_i(x_0) = \lambda_i(x_0) - \lambda^2$, some of which will

typically be positive and the others negative. The tensor fields $C(x_0)$ and $E_\lambda(x_0)$ remain invariant under Euclidean changes of coordinates and hence are objective.

3.3. Computing the Deformation Gradient

Neither the flow map nor its gradient is objective, but both are necessary for computing $C(x_0)$ and $E_\lambda(x_0)$. Solving Equation 4 directly tends to give noisy results for $\nabla F_{t_0}^t(x_0)$ as a function of x_0. Instead, for Lagrangian coherence calculations, Haller (2001a) proposed using the finite-difference approximation

$$\nabla F_{t_0}^t(x_0) \approx \begin{pmatrix} \frac{x^1(t;t_0,x_0+\delta_1)-x^1(t;t_0,x_0-\delta_1)}{|2\delta_1|} & \frac{x^1(t;t_0,x_0+\delta_2)-x^1(t;t_0,x_0-\delta_2)}{|2\delta_2|} & \frac{x^1(t;t_0,x_0+\delta_3)-x^1(t;t_0,x_0-\delta_3)}{|2\delta_3|} \\ \frac{x^2(t;t_0,x_0+\delta_1)-x^2(t;t_0,x_0-\delta_1)}{|2\delta_1|} & \frac{x^2(t;t_0,x_0+\delta_2)-x^2(t;t_0,x_0-\delta_2)}{|2\delta_2|} & \frac{x^2(t;t_0,x_0+\delta_3)-x^2(t;t_0,x_0-\delta_3)}{|2\delta_3|} \\ \frac{x^3(t;t_0,x_0+\delta_1)-x^3(t;t_0,x_0-\delta_1)}{|2\delta_1|} & \frac{x^3(t;t_0,x_0+\delta_2)-x^3(t;t_0,x_0-\delta_2)}{|2\delta_2|} & \frac{x^3(t;t_0,x_0+\delta_3)-x^3(t;t_0,x_0-\delta_3)}{|2\delta_3|} \end{pmatrix}, \quad (9)$$

with a small vector δ_i pointing in the x^i coordinate direction. For two-dimensional flows, only the first 2×2 minor matrix of Equation 9 is relevant.

The computational cost of evaluating Equation 9 can be prohibitive in three dimensions. With an emphasis on computing the largest singular value of $\nabla F_{t_0}^t(x_0)$, Shadden (2012) and Peikert et al. (2014) give excellent surveys of related numerical methods.

Two-dimensional approximations to $\nabla F_{t_0}^t(x_0)$ also reduce the computational cost. One may confine the numerical grid to two-dimensional surfaces and compute the directional derivatives of $F_{t_0}^t(x_0)$ only along these surfaces (Garth et al. 2007). Alternatively, one may ignore vertical velocities (but not the variation of horizontal velocities) in stratified flows, rendering the last row of the deformation gradient in Equation 9 zero (Sulman et al. 2013).

As a new approach, Leung (2011, 2013) proposes a partial differential equation–based computation of the flow map using a level-set approach. This technique requires no velocity interpolation, but its advantages and accuracy have yet to be demonstrated beyond simple kinematic models. In an experimental setting, Raben et al. (2014a,b) consider the direct numerical reconstruction of the flow gradient $\nabla F_{t_0}^t(x_0)$ from observed particle tracks.

Fluid trajectories may leave the computational domain prematurely in velocity fields with limited spatial coverage. Issues created by this fact and a way to address them are discussed by Tang et al. (2010a, 2011a,b) and Kafiabad et al. (2013) with applications to wind fields measured over airports.

3.4. Material Advection

Once an influential material surface is identified as an LCS at time t_0, its later positions are determined by advection under the flow map, as in Equation 5. For two-dimensional flows, Mancho et al. (2003) compare numerical methods for accurate material line advection. For three-dimensional flows, Branicki & Wiggins (2009) develop an adaptive numerical method for accurate material surface advection. Recent approaches render initial LCS positions explicitly as parameterized lines and surfaces (see Sections 5 and 6), which aids their numerical advection as material surfaces.

3.5. Forward-Backward Time Duality

Earlier approaches to LCSs focused on locating material instabilities that prevail in forward-time applications of the flow map. Identifying attracting material structures at time t_0 for a flow known over $[t_0, t_1]$ was only thought possible from a separate backward-time calculation from t_0.

Alternatively, both attracting and repelling LCSs were computed at time $(t_0 + t_1)/2$ from separate forward and backward calculations over half of the available data. As a drawback, the first approach requires the velocity field prior to t_0 to be available. In addition, both approaches effectively analyze different finite-time dynamical systems in forward and backward time yet superimpose the conclusions for these different systems.

More recent results (Haller & Sapsis 2011, Farazmand & Haller 2013, Karrasch 2013, Blazevski & Haller 2014) highlight a duality principle between the backward- and forward-time flow map, enabling the computation of all relevant material surfaces from a single numerical run.

3.6. Computing the Invariants of $C(x_0)$

Diagnostic approaches to LCS computation (see Section 4) focus on spatial features in the dominant eigenvalue field of $C(x_0)$. As shown by Haller (2002), the location of these features is surprisingly robust under numerical and measurement errors, even if the actual numerical values of the eigenvector field are inaccurate.

More recent approaches to LCS also require the accurate computation of the eigenvalues and eigenvectors of $C(x_0)$. This necessitates the use of auxiliary grids for differentiation, and the orientation and desingularization of the strain eigenvector field for the purposes of tensor-line calculations (see Sections 5 and 6).

4. THE FINITE-TIME LYAPUNOV EXPONENT: AN OBJECTIVE DIAGNOSTIC FOR LAGRANGIAN COHERENT STRUCTURES

4.1. Motivation

Locating LCSs would normally require a detailed assessment of the stability of material surfaces in the flow domain of interest. A first-order approach to this problem simply involves the detection of material surfaces along which infinitesimal deformation is larger or smaller than off these surfaces.

To this end, we seek the initial position $\mathcal{M}(t_0)$ of a material surface $\mathcal{M}(t)$ along which infinitesimal spheres stretch the most by time t_1. As illustrated in **Figure 4**, the largest possible stretching at a point x_0 is given by $\sqrt{\lambda_n(x_0)}$, which typically grows exponentially. The average exponent of this growth can be determined as

$$\Lambda_{t_0}^{t_1}(x_0) = \frac{1}{t_1 - t_0} \log \sqrt{\lambda_n(x_0)},$$

known as the FTLE at the initial position x_0.

The initial position $\mathcal{M}(t_0)$ of an LCS can then be sought as an extremizing surface (a ridge or a trench) of the scalar field $\Lambda_{t_0}^{t_1}(x_0)$. Several contested mathematical definitions exist for ridges. Here, I state only informally that a ridge of a scalar field is a hypersurface along which one sees a smaller change in the value of the scalar than in directions transverse to the ridge. A trench can then be defined as a ridge of the negative of the scalar field. The recent ridge definition of Karrasch & Haller (2013) guarantees the structural stability of the FTLE ridge under perturbation, which is suitable for LCS analysis of flow data with noise.

4.2. History

Plots of $\Lambda_{t_0}^{t}(x_0)$ over initial conditions as indicators of mixing regions already have been provided by Pierrehumbert & Yang (1993), followed by von Hardenberg et al. (2000). Doerner et al. (1999)
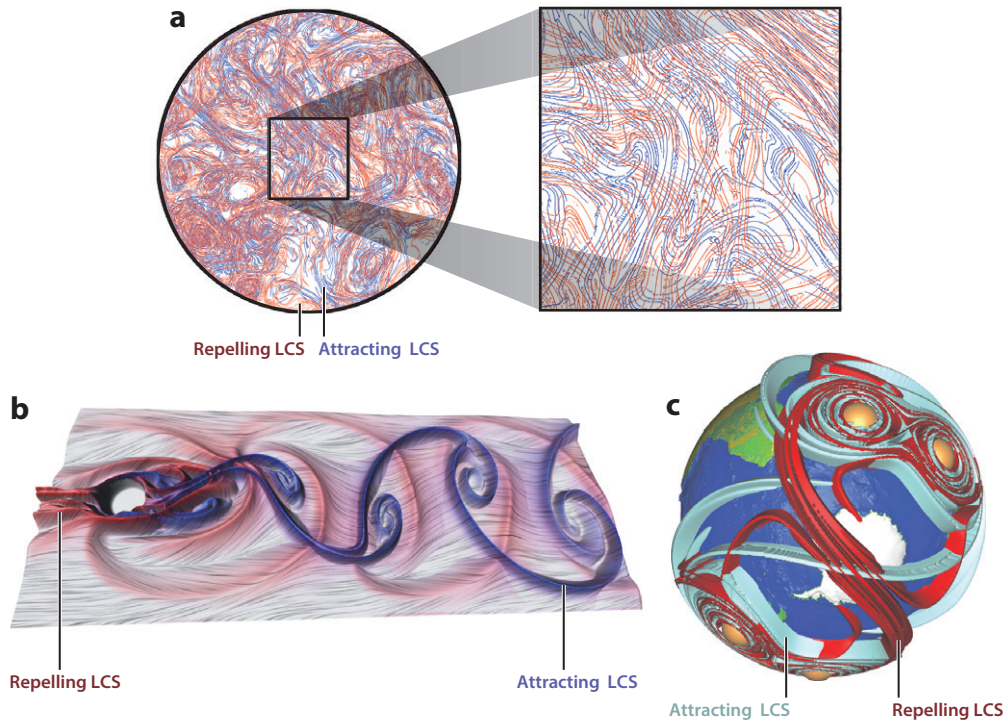
Figure 5

(*a*) The Lagrangian skeleton of turbulence in a two-dimensional rotating flow experiment. Repelling Lagrangian coherent structure (LCS) candidates (*red*) are ridges of the forward-time finite-time Lyapunov exponent (FTLE). Attracting LCS candidates (*blue*) are ridges of the backward-time FTLE. Panel *a* reproduced with permission from Mathur et al. (2007). (*b*) A similar computation for the von Kármán vortex street behind a cylinder, with the height of the gray surface representing the maximum of forward- and backward-time FTLEs. Panel *b* reproduced with permission from Kasten et al. (2010). (*c*) Repelling (*red*) and attracting (*blue*) LCSs for a perturbed four-vortex-ring model for the 2002 splitting of the Antarctic ozone hole. Panel *c* reproduced with permission from Lekien & Ross (2010).

also note that contours of the FTLE align closely with unstable manifolds of classic, infinite-time dynamical systems.

Provenzale (1999) and Bowman (2000) put forward the idea to use relative dispersion, a discretized form of the FTLE, to highlight Lagrangian features. Although relative dispersion as a statistical tool has well-established properties (LaCasce 2008), its spatially discretized nature has prevented attempts to relate its features mathematically to the stability of material surfaces.

The first works connecting FTLE ridges to repelling LCSs through the above heuristic argument were by Haller (2001a, 2002). Next, the FTLE was applied to LCS extraction from time-periodic laboratory experiments by Voth et al. (2002) and then from turbulent flow experiments by Mathur et al. (2007), shown in **Figure 5*a***. Further high-end visualizations of LCSs via FTLE ridges by Kasten et al. (2010) and Lekien & Ross (2010) are shown in **Figure 5*b*,*c***.

A number of applications to numerical and experimental data followed, as surveyed by Peacock & Dabiri (2010), Shadden (2012), and Peacock & Haller (2013). Recent studies of LCSs in astrophysical plasmas via FTLE ridges appear in Yeates et al. (2012), Rempel et al. (2013), and Chian et al. (2014). Experimental work by Kelley et al. (2013) suggests that FTLE ridges also tend to mark the zeros of scale-to-scale energy flux in weakly turbulent, two-dimensional flows.

Mathematical criteria relating FTLE ridges to repelling LCS were obtained by Haller (2002, 2011), Farazmand & Haller (2012b), Tang et al. (2011b), and Karrasch (2012), with applications by Mathur et al. (2007), Green et al. (2007, 2010, 2011), and Tang et al. (2010b, 2011a,b).

Another related Lagrangian indicator, FSLEs, was originally conceived to study finite-size material perturbations in a statistical fashion (Aurell et al. 1997). However, Joseph & Legras (2002), d'Ovidio et al. (2004), Bettencourt et al. (2013), and others also employ FSLEs in LCS detection, assuming an equivalence between ridges of the FSLE and FTLE fields. Scrutinizing this assumption, Karrasch & Haller (2013) find that only FSLE ridges with moderate variation in their height are guaranteed to signal nearby FTLE ridges. Peikert et al. (2014) argue that computational advantages attributed to FSLEs over FTLEs in earlier studies originate from poor parameter choices and sampling artifacts.

Beron-Vera et al. (2010, 2012) focus specifically on trenches of the FTLE field. They observe that trenches coinciding in forward and backward FTLE calculations mark shearless invariant tori (zonal jet cores) in spatially periodic geophysical flows. Haller & Sapsis (2011) show that trenches of the FTLE field graphed over time t_1 fluid positions mark attracting LCSs at time t_1.

4.3. Issues with Finite-Time Lyapunov Exponents

Without the additional mathematical criteria mentioned in Section 4.2, the FTLE approach to hyperbolic LCS detection is heuristic. It ignores the direction $\xi_n(x_0)$ of largest stretching at x_0, which may well be along or close to directions tangent to $\mathcal{M}_0$. Indeed, Haller (2002, 2011) gives examples of FTLE ridges along shearing surfaces. Branicki & Wiggins (2010) further illustrate inconsistencies between hyperbolic LCS and the FTLE field on simple examples. Karrasch (2013) shows that attracting LCSs of incompressible flows are also ridges of the FTLE field, but they are invariably missed because of finite numerical resolution.

Shadden et al. (2005, 2007) seem to resolve these mathematical questions simply by defining an LCS, $\hat{\mathcal{M}}(t)$, as a second-derivative ridge of the FTLE field $\Lambda_t^{t+T}(x_0)$ for evolving times t and fixed integration time T. The $\hat{\mathcal{M}}(t)$ family so defined, however, does not satisfy the invariance requirement in Equation 5, as illustrated in Section 2.3. To this end, Shadden et al. (2005) provide a flux formula that suggests small material flux through $\hat{\mathcal{M}}(t)$. Lipinski & Mohseni (2010) use this formula to derive a further measure of how close $\hat{\mathcal{M}}(t)$ is to being Lagrangian.

These ideas have since turned out to be problematic upon closer examination. Second-derivative FTLE ridges do not exist in generic fluid flows (Norgard & Bremer 2012, Schindler et al. 2012), and the flux formula of Shadden et al. (2005, 2007) derived for such ridges is generally invalid (Haller 2011). For the two-dimensional steady flow in **Figure 3c**, for instance, the flux formula of Shadden et al. (2005) predicts zero leading-order flux per unit length through the FTLE ridge at $x = 0$. The actual material flux, however, is equal to one.

Although FTLE plots remain popular visual diagnostics of Lagrangian coherence, more reliable mathematical methods have been developed for the explicit identification of LCSs as parameterized material surfaces. These material surfaces now also include elliptic LCSs (Lagrangian vortices) and parabolic LCSs (Lagrangian jet cores), beyond the hyperbolic LCSs originally targeted by the FTLE approach. I survey these results in Sections 5 and 6 below.

5. LOCAL THEORY OF LAGRANGIAN COHERENT STRUCTURES

The local theory of LCSs builds on their original definition as the pointwise strongest repelling, attracting, or shearing material surfaces in the flow over a time interval of interest. At an initial point x_0, we let n_0 denote a unit normal to an initial material surface $\mathcal{M}(t_0)$, as in **Figure 6**. While
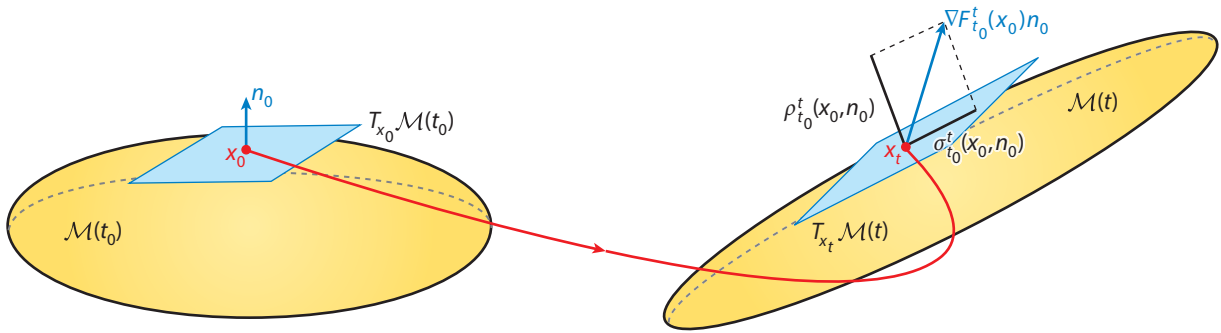
Figure 6

Quantifying normal repulsion and tangential shear along an evolving material surface $\mathcal{M}(t)$.

the tangent plane of $\mathcal{M}(t_0)$ is mapped into a tangent space of the deformed surface $\mathcal{M}(t_1)$ by the linearized flow map $\nabla F_{t_0}^{t_1}(x_0)$, the advected normal $\nabla F_{t_0}^{t_1}(x_0)n_0$ generally does not remain normal to $\mathcal{M}(t_1)$. In addition to a normal component of length $\rho(x_0, n_0)$, the advected normal also has a tangential component of length $\sigma(x_0, n_0)$, as shown in **Figure 6**.

If $\rho(x_0, n_0) > 1$, then the evolving material surface exerts net normal repulsion on nearby fluid elements. Similarly, $\rho(x_0, n_0) < 1$ signals that the material surface attracts fluid elements along its normal direction. In contrast, $\sigma(x_0, n_0) > 0$ indicates shear exerted by $\mathcal{M}(t)$ on nearby fluid elements, as first noted by Tang et al. (2011a) for two-dimensional flows.

These geometric concepts enable a precise definition of LCSs. Specifically, a repelling (attracting) LCS over the interval $[t_0, t_1]$ is a material surface $\mathcal{M}(t)$ whose net repulsion $\rho(x_0, n_0)$ is pointwise maximal (minimal) with respect to perturbations of the initial normal vector field n_0. I refer to repelling and attracting LCSs collectively as hyperbolic LCSs. Similarly, a shear LCS over the interval $[t_0, t_1]$ is a material surface $\mathcal{M}(t)$ whose net shear $\sigma(x_0, n_0)$ is pointwise maximal with respect to perturbations of the initial normal vector field n_0.

Farazmand & Haller (2012a, 2013) and Blazevski & Haller (2014) find that the initial positions of hyperbolic and shear LCSs must necessarily be orthogonal to specific vector fields, as detailed in the $n = 2, 3$ column of **Table 1**. The shear normal vector field $n_\pm$ appearing in this column is given by

$$n_\pm(x_0) = \sqrt{\frac{\sqrt{\lambda_1(x_0)}}{\sqrt{\lambda_1(x_0)} + \sqrt{\lambda_n(x_0)}}}\xi_1(x_0) \pm \sqrt{\frac{\sqrt{\lambda_n(x_0)}}{\sqrt{\lambda_1(x_0)} + \sqrt{\lambda_n(x_0)}}}\xi_n(x_0). \qquad (10)$$

Later positions of the LCS within the time interval $[t_0, t_1]$ can be obtained by Lagrangian advection, as described in Equation 5. The local approach described here can also be used to develop detection methods for hyperbolic LCSs in higher-dimensional ($n \geq 3$) steady flows (Teramoto et al. 2013).

5.1. Lagrangian Coherent Structures in Two-Dimensional Flows

For two-dimensional flows ($n = 2$), the normals shown in the first column of **Table 1** uniquely define the tangents of LCSs, thus providing differential equations that these LCSs must solve (Farazmand & Haller 2012a, 2013; Haller & Beron-Vera 2012). The $n = 2$ column of **Table 1** summarizes the corresponding ordinary differential equations (ODEs).

These differential equations reveal a foliation of the fluid flow by LCS curves. Indeed, the trajectories of $\dot{r} = \xi_1(r)$ (shrink lines) and those of $\dot{r} = \xi_2(r)$ (stretch lines) decompose the full material deformation into attractive and repulsive components. One obtains a skeleton of the

Table 1 Local constraints on the initial position $\mathcal{M}(t_0)$ of a Lagrangian coherent structure (LCS) over the time interval $[t_0, t_1]$

LCS	$n = 2, 3$	$n = 2$	$n = 3$	
	Normal to $\mathcal{M}(t_0)$	ODE for $\mathcal{M}(t_0)$	ODE for $\mathcal{M}(t_0) \cap \Pi$	$\mathcal{M}(t_0)$ location
Attracting	$\xi_1(x_0)$	$\dot{r} = \xi_2(r)$	$r' = n_\Pi(r) \times \xi_1(r)$	$\langle \nabla \times \xi_1, \xi_1 \rangle = 0$
Repelling	$\xi_n(x_0)$	$\dot{r} = \xi_1(r)$	$r' = n_\Pi(r) \times \xi_3(r)$	$\langle \nabla \times \xi_3, \xi_3 \rangle = 0$
Shear	$n_\pm(x_0)$	$\dot{r} = \eta^\pm(r)$	$r' = n_\Pi(r) \times n_\pm(r)$	$\langle \nabla \times n_\pm, n_\pm \rangle = 0$

The eigenvalues λ_i and eigenvectors ξ_i featured in the formulae are those of the Cauchy-Green strain tensor C. The dimension of the flow is n. Abbreviation: ODE, ordinary differential equation.

most influential hyperbolic LCS by finding the locally most repelling shrink lines and the locally most attracting stretch lines, as described by Farazmand & Haller (2012a). A more efficient recent approach finds the most influential hyperbolic LCSs as shrink lines through local maxima of $\lambda_2(x_0)$ and stretch lines through local minima of $\lambda_1(x_0)$ (Onu et al. 2014).

The trajectories of $\dot{r} = \eta^\pm(r)$ (shear lines) mark the fundamental geometry of shearing patterns, with the shear vector field defined as

$$\eta^\pm(r) := \sqrt{\frac{\sqrt{\lambda_2(x_0)}}{\sqrt{\lambda_1(x_0)} + \sqrt{\lambda_2(x_0)}}} \xi_1(x_0) \pm \sqrt{\frac{\sqrt{\lambda_1(x_0)}}{\sqrt{\lambda_1(x_0)} + \sqrt{\lambda_2(x_0)}}} \xi_2(x_0). \tag{11}$$

Remarkably, any piece of a shear line advected in an incompressible flow has the exact same arc length at time t_1 as at time t_0 (Haller & Beron-Vera 2012). This conservation property gives special significance to closed shear lines [i.e., limit cycles of $\dot{r} = \eta^\pm(r)$]. In incompressible flows, both the arc length and the interior area of these closed curves are preserved by the flow map $F_{t_0}^{t_1}$, making closed shear lines the time-aperiodic analogs of the KAM curves known from time-periodic flows (see **Figure 2**). For this reason, I refer to closed shear lines as elliptic LCSs. Furthermore, I consider the outermost member of a nested elliptic LCS family to be the boundary of a coherent Lagrangian vortex (see Section 6 for a generalization of this idea).

Figure 7 illustrates LCSs computed as shrink lines, stretch lines, and shear lines in a velocity field obtained from a direct numerical simulation of forced, two-dimensional turbulence. Applications to ocean data are provided by Olascoaga & Haller (2012), Beron-Vera et al. (2013), and Olascoaga et al. (2013).

A MATLAB implementation of two-dimensional local LCS results (LCS Tool) surveyed here is available at **https://github.com/jeixav/LCS-Tool**, with a detailed description given by Onu et al. (2014).

In related work, Ma & Bollt (2013) seek shape-coherent set boundaries as locations where the forward- and backward-time dominant strain eigenvectors enclose a minimal angle. This approach tacitly assumes that strain eigenvectors obtained via a backward-time analysis starting from time t_0 will continue to play a distinguished role after t_0. In recurrent model flows, this procedure is indeed expected to yield sets of curves close to the LCSs described in **Table 1**. In nonrecurrent flows, however, shape-coherent boundaries will generally not mark LCSs for the reasons described in Section 3.5.

5.2. Lagrangian Coherent Structures in Three-Dimensional Flows

In three dimensions ($n = 3$), surfaces orthogonal to a given vector field may only exist where the helicity of the vector field vanishes (Palmerius et al. 2009). Accordingly, LCS initial positions
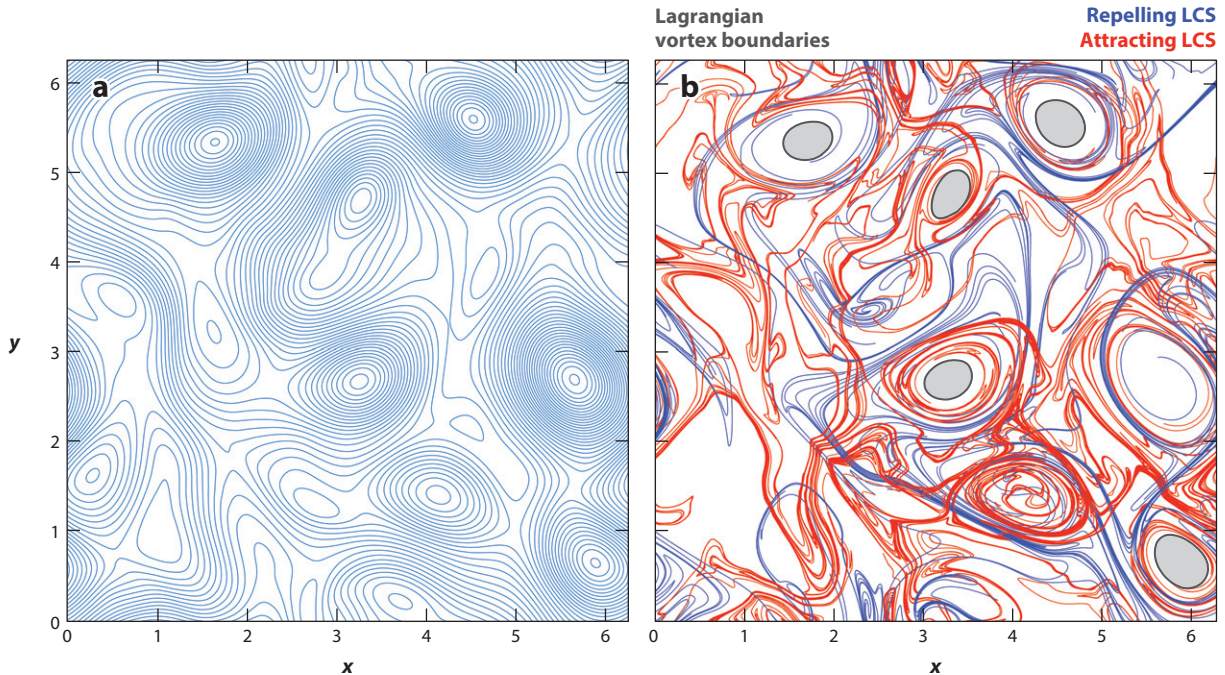
Figure 7

Hyperbolic and elliptic Lagrangian coherent structures (LCSs) in a direct numerical simulation of two-dimensional forced turbulence. (*a*) Instantaneous streamlines. (*b*) Repelling LCS (*blue*), attracting LCS (*red*), and Lagrangian vortex boundaries (with *gray interior*) at the same time instance. Figure adapted from Farazmand & Haller (2014).

satisfying the general orthogonality constraints given in **Table 1** may exist only at the locations summarized in the second $n = 3$ column of **Table 1**.

Blazevski & Haller (2014) derive ODEs for the intersection curves of initial LCS surfaces with an arbitrary two-dimensional surface Π selected for visualization purposes (see the first $n = 3$ column in **Table 1**). They call the trajectories of these ODEs reduced stretch lines, reduced shrink lines, and reduced shear lines, respectively (see **Figure 8a**). These lines are the simplest to compute when Π is a plane, and hence the normal n_Π does not depend on the location r.

In locating LCSs, one selects the trajectories of the above ODEs on which the corresponding zero helicity conditions hold with the highest accuracy. This process provides isolated intersection curves between initial LCS positions $\mathcal{M}(t_0)$ and the surface Π. Fitting a smooth surface to such intersection curves obtained for a whole family of Π surfaces provides a numerical approximation to $\mathcal{M}(t_0)$. This process reveals sharply defined elliptic barriers in the chaotically forced ABC flow (**Figure 8b**) that defy the intense deformation experienced by nearby fluid elements (**Figure 8c**). Finally, **Figure 8d** shows how the same approach yields coherent cylindrical Lagrangian eddy boundaries in the three-dimensional oceanic Southern Ocean State Estimate data set (Mazloff et al. 2010).

6. GLOBAL THEORY OF LAGRANGIAN COHERENT STRUCTURES

The local approach surveyed in the previous section finds LCSs as material surfaces with locally maximal repelling, attracting, or shearing impact on neighboring fluid elements. For
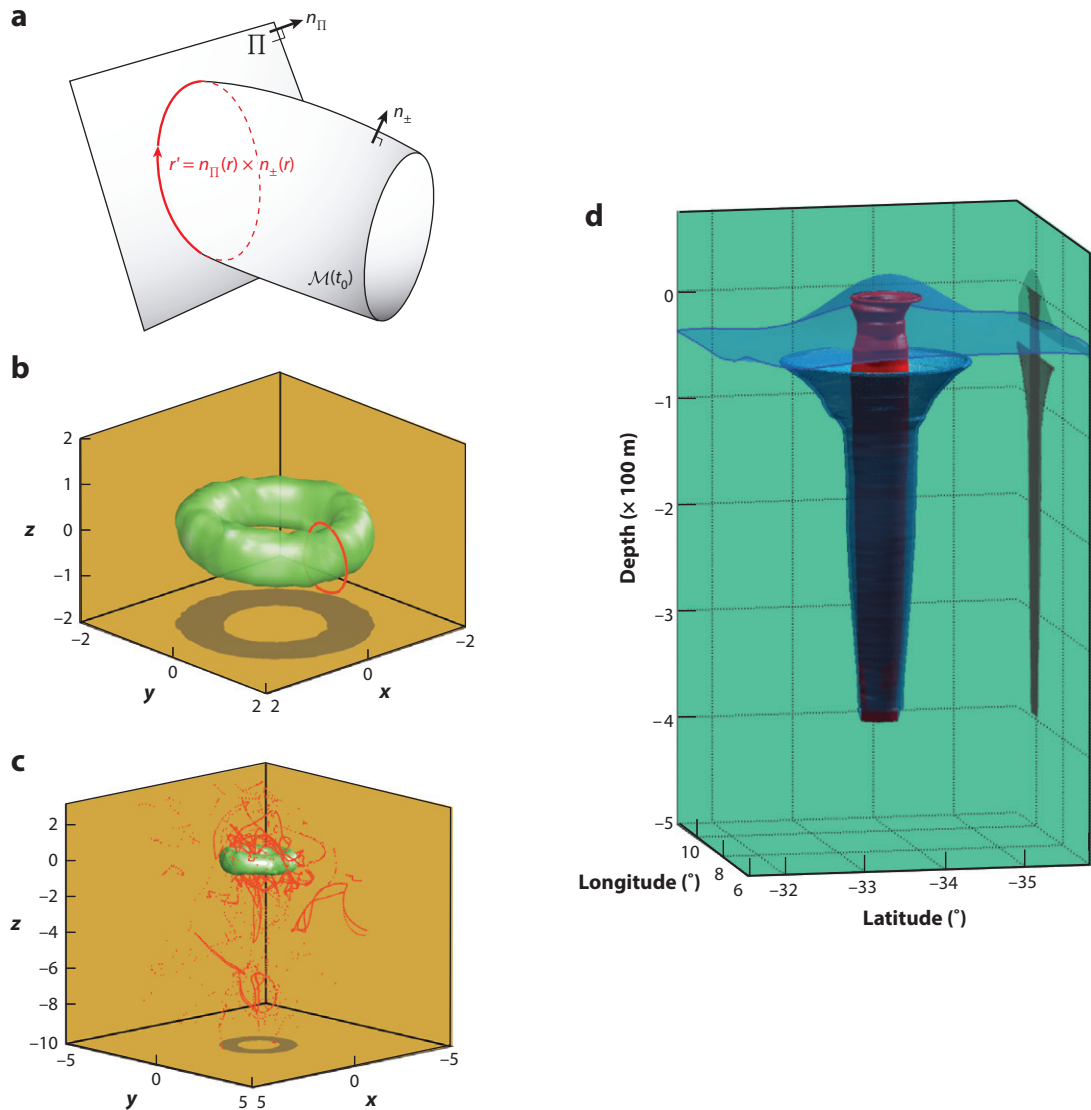
Figure 8

Construction of a shear Lagrangian coherent structure (LCS) in three-dimensional unsteady flows. (*a*) The geometry of reduced shear lines on a plane Π intersecting the initial LCS position $\mathcal{M}(t_0)$ transversely. (*b*) Elliptic LCS (toroidal shear LCS) in the chaotically forced ABC flow, extracted over the time interval [0, 10]. A circular ring (*red*) is initialized slightly outside of the LCS for later reference. (*c*) The material evolution of the elliptic LCSs (eddy core and outer boundary) and the ring under the flow map F_0^{15}, showing the coherence of the LCS to be atypical. (*d*) Cylindrical elliptic LCS extracted from the Southern Ocean State Estimate data set. Panels *a–c* reproduced with permission from Blazevski & Haller (2014). Panel *d* courtesy of Daniel Blazevski.

two-dimensional flows, global variational principles are now also available, targeting LCSs as material lines with exceptional global coherence properties. As shown below, these global approaches recover the results of local LCS theory but also reveal further LCSs, such as weakly but coherently stretching material vortices and Lagrangian jet cores.

6.1. Lagrangian Coherent Structures as Extremum Curves of Absolute Deformation

Instead of characterizing the impact of LCSs on nearby material curves, one may focus on the internal dynamics of LCSs. Motivated by the classic planar invariant manifolds shown in **Figure 2**, Haller & Beron-Vera (2012) propose to find repelling and shear LCSs in planar flows as least-stretching material lines. Similarly, attracting LCS may be sought as least-stretching curves in backward time over the same time interval.

The initial positions of least-stretching material lines turn out to be geodesics of the Riemannian metric $c(u, v) = \langle u, Cv \rangle$ induced by the Cauchy-Green strain tensor C. These geodesics all deform to straight lines under the flow map $F_{t_0}^{t_1}$ and thus are generally inconsistent with LCSs obtained from the local theory in Section 5. Nevertheless, the boundary conditions arising in the variational principle put forward by Haller & Beron-Vera (2012) suggested a global role of stretch lines and shrink lines, which was subsequently confirmed by the geodesic LCS methods surveyed below.

6.2. Lagrangian Coherent Structures as Stationary Curves of Relative Deformation

The deformation of a general material element is subject to simultaneous straining and shearing. In a smooth flow, the averaged straining and shearing along two, ϵ-close material lines will differ by an $\mathcal{O}(\epsilon)$ amount over a finite time interval.

We may seek an LCS as an exceptional material curve whose ϵ-close neighbors show no $\mathcal{O}(\epsilon)$ change in their averaged straining or shearing values. This means that the average shearing or straining across the LCS varies significantly less than what is expected near a generic material curve.

6.2.1. Stationary curves of average shear: hyperbolic and parabolic Lagrangian coherent structures. A stationary shear LCS is a centerpiece of a thin strip of material lines whose averaged Lagrangian shear (see **Figure 6**) shows an order of magnitude less variation than what the width of the region would generally warrant. Working out the details of this definition, Farazmand et al. (2014) obtain that such stationary shear LCSs coincide with null geodesics of the Lorentzian metric

$$g(u, v) = \langle u, Dv \rangle, \quad D(x_0) = \frac{1}{2}[C(x_0)\Omega - \Omega C(x_0)], \quad \Omega = \begin{pmatrix} 0 & -1 \\ 1 & 0 \end{pmatrix}. \quad (12)$$

It turns out that any such null geodesic is composed of shrink lines and stretch lines, as listed in the second column of **Table 2**.

Table 2 Conditions for a Lagrangian coherent structure (LCS) obtained as a geodesic of the Lorentzian deformation metric $g(u, v)$

Type of 2D geodesic LCS	$\mathcal{M}(t_0)$ solves	Boundary condition
Hyperbolic, attracting	$\dot{r} = \xi_2(r)$	Fixed with $C \neq I$
Hyperbolic, repelling	$\dot{r} = \xi_1(r)$	Fixed with $C \neq I$
Parabolic	$\dot{r} = \xi_2(r)$ alternating with $\dot{r} = \xi_1(r)$	Variable with $C = I$
Elliptic	$\dot{r} = \eta_\lambda^\pm(r)$	Periodic

The eigenvalues λ_i and eigenvectors ξ_i are those considered in **Table 1**. The vector fields $\eta_\lambda^\pm(r)$ are defined in Equation 14.

Hyperbolic LCSs re-emerge from this stationary shear approach as individual shrink line or stretch line trajectory segments between end points for which $C \neq I$ holds. Such segments, however, are only stationary curves of the averaged shear under special variations that leave their end points fixed.

In contrast, a parabolic LCS (or generalized jet core) is a smooth, alternating chain of shrink lines and stretch lines that connects points for which $C = I$. Out of all such chains, only those qualify as LCSs that are also weak minimizers of the neutrality, a measure of how close the LCS is as a whole to being neutrally stable (Farazmand et al. 2014).

Remarkably, such stretch-shrink chains are stationary curves of the averaged shear with respect to all variations, including those that perturb their end points. This implies that parabolic LCSs should prevail in tracer patterns more strongly than hyperbolic LCSs. Indeed, as **Figure 1** illustrates, jet cores tend to have sharper centerpieces than hyperbolic LCSs in geophysical observations. The last column of **Table 2** summarizes the boundary conditions of shearless geodesic LCSs.

Figure 9c shows the geodesic extraction of the Lagrangian jet core (parabolic LCS) surrounding the Antarctic stratospheric polar vortex. Hadjighasem & Haller (2014a,b) identify parabolic LCSs acting as material cores of zonal jets in the atmosphere of Jupiter (see **Figure 9d**).
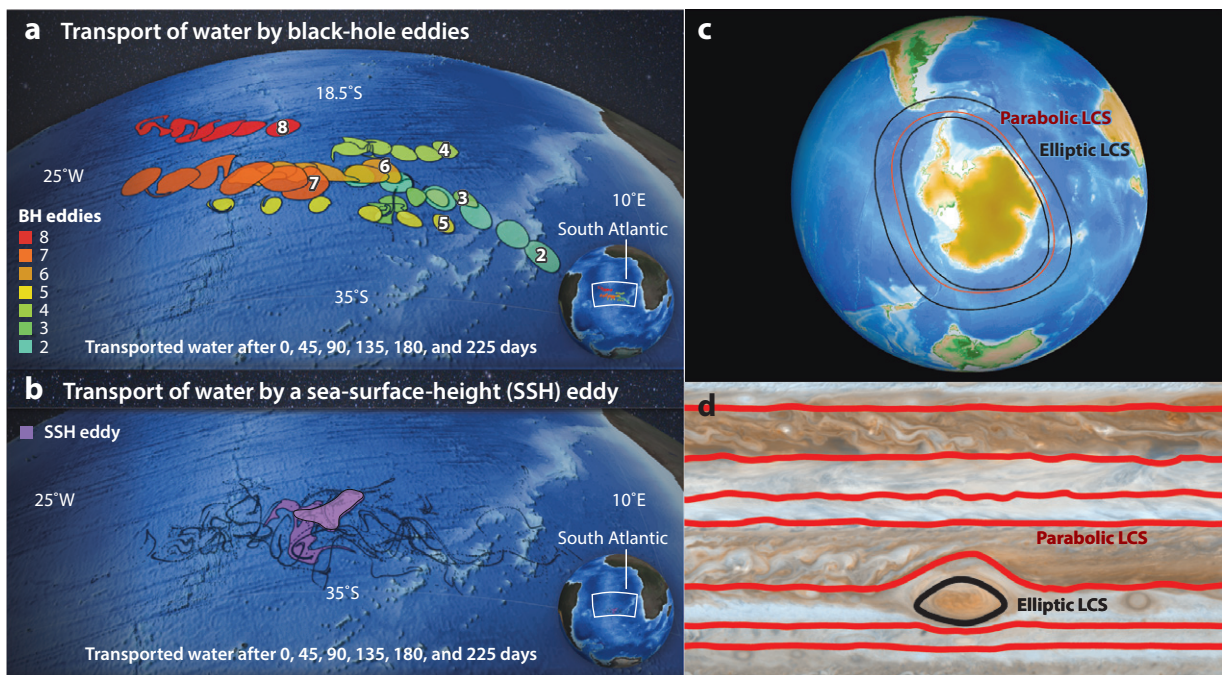

Figure 9

Geodesic Lagrangian coherent structure (LCS) detection from geophysical data. (*a*) Black-hole-type eddies in the southern Atlantic Ocean, extracted from three months of satellite altimetry velocities and then advected over nine months. (*b*) The Lagrangian evolution of fluid in a coherent eddy identified from the same data by the Eulerian algorithm of Chelton et al. (2011). Panel *b* reproduced with permission from Haller & Beron-Vera (2013). Copyright Cambridge University Press. (*c*) Parabolic LCS (*red*) serving as the Lagrangian core of a zonal jet encircling the Antarctic polar vortex in the Canadian Middle Atmosphere Model. Also shown are two elliptic LCSs (*black*) forming the boundaries of the jet. Panel *c* courtesy of Mohammad Farazmand. (*d*) Parabolic LCS (*red*) as zonal jet cores and an elliptic LCS (*black*) forming the Lagrangian boundary of the Great Red Spot of Jupiter. The time-resolved velocity field used in the analysis is extracted from video footage of the NASA Cassini mission using the ACCIV algorithm of Asay-Davis et al. (2009). Image from NASA, reproduced from Hadjighasem & Haller (2014a).

6.2.2. Stationary curves of average strain: elliptic Lagrangian coherent structures. A stationary-strain shear LCS is a centerpiece of a thin strip of material lines whose averaged normal repulsion (see **Figure 6**) shows an order of magnitude less variation than what the width of the region would generally warrant. In incompressible flows, this is equivalent to the requirement that the averaged tangential stretching of the LCS shows no leading-order change across neighboring material curves.

As shown by Haller & Beron-Vera (2013, 2014), stationary curves of the tangential stretching functional coincide with null geodesics of the Lorentzian metric family,

$$g_\lambda(u, v) = \langle u, E_\lambda v \rangle, \quad \lambda > 0, \tag{13}$$

with the generalized Green-Lagrange strain tensor $E_\lambda(x_0)$ defined in Equation 8. Such null geodesics are tangent to one of the vector fields

$$\eta_\lambda^\pm(x_0) = \sqrt{\frac{\lambda_2(x_0) - \lambda^2}{\lambda_2(x_0) - \lambda_1(x_0)}} \xi_1(x_0) \pm \sqrt{\frac{\lambda^2 - \lambda_1(x_0)}{\lambda_2(x_0) - \lambda_1(x_0)}} \xi_2(x_0), \tag{14}$$

with λ_i and ξ_i defined in Equation 7. I refer to closed orbits of the vector fields (Equation 14) as elliptic LCSs (see **Table 2**).

As null geodesics of a Lorentzian metric that have periodic space-like projections, limit cycles of $\eta_\lambda^\pm$ are mathematically equivalent to photon spheres (Claudel et al. 2001) surrounding black holes in general relativity. This analogy implies the necessary existence of a metric singularity (a point for which $C = I$) within each elliptic LCS, which in turn expedites the detection of such LCSs in large velocity data sets (Haller & Beron-Vera 2013, Karrasch et al. 2014).

Selecting the outermost member of a family of λ-dependent limit cycles generalizes the idea of a Lagrangian vortex boundary from outermost nonstretching cycles ($\lambda = 1$ in Section 5.1) to outermost uniformly stretching cycles. By the cosmological analogy between uniformly stretching vortex boundaries and photon spheres, material eddies encircled by maximal limit cycles of Equation 14 may be referred to as black-hole eddies.

Black-hole eddies reveal the exact Lagrangian footprints (**Figure 9a**) of coherent Agulhas rings, such as the one inferred from **Figure 1f**. This in turn provides specific transport estimates for the coherent part of the Agulhas leakage (Haller & Beron-Vera 2013). A further high-profile example identified by Hadjighasem & Haller (2014a,b) is the coherent material core of Jupiter's Great Red Spot (see **Figure 9d**).

7. SUMMARY AND OUTLOOK

The tool kit for the detection of Lagrangian coherent structures has matured to a level allowing the full Lagrangian skeleton of a general turbulent flow to be determined over a finite time interval of interest (compare **Figure 1** with **Figures 7–9**).

Indeed, LCSs can now be accurately identified from experimental data (Voth et al. 2002; Mathur et al. 2007; Raben et al. 2014a,b); coherent Lagrangian eddy transport in ocean models can readily be quantified (Beron-Vera et al. 2013); detailed Lagrangian now-casting for the ocean and atmosphere is within reach (Tang et al. 2011a,b; Shuckburgh 2012; Bozorgmagham et al. 2013); and LCS-based short-term forecasting has become a reality (Coulliette et al. 2007, Olascoaga & Haller 2012, Olascoaga et al. 2013).

Recent developments promise much needed improvement in computational efficiency and visualization (Garth et al. 2007, Sadlo & Peikert 2007, Sadlo et al. 2010, Brunton & Rowley 2010, Barakat et al. 2012, Conti et al. 2012). These advances will be critical to three-dimensional LCS computations targeting specific material surfaces.

Further work is required to explore the relation of the geometric LCS methods surveyed here to topological (Allshouse & Thiffeault 2012), ergodicity-based (Budišić & Mezić 2012), observer-based (Mezić 2013), and probabilistic (Froyland & Padberg-Gehle 2014) approaches that target domains enclosed by LCSs. Finally, promising extensions of LCS concepts for passive tracers are underway for finite-size particle motion (Peng & Dabiri 2009, Sapsis et al. 2011) and for reactive front propagation (Mahoney et al. 2012, Mitchell & Mahoney 2012).

DISCLOSURE STATEMENT

The author is not aware of any biases that might be perceived as affecting the objectivity of this review.

ACKNOWLEDGMENTS

LITERATURE CITED

Allshouse MR, Thiffeault JL. 2012. Detecting coherent structures using braids. *Physica D* 241:95–105

Arnold VI. 1973. *Ordinary Differential Equations*. Cambridge, MA: MIT Press

Asay-Davis XS, Marcus PS, Wonga MH, de Patera I. 2009. Jupiter's shrinking Great Red Spot and steady Oval BA: velocity measurements with the 'Advection Corrected Correlation Image Velocimetry' automated cloud-tracking method. *Icarus* 203:164–88

Aurell E, Boffetta G, Crisanti A, Paladin G, Vulpiani A. 1997. Predictability in the large: an extension of the concept of Lyapunov exponent. *J. Phys. A* 30:1–26

Barakat S, Garth C, Tricoche X. 2012. Interactive computation and rendering of Finite-Time Lyapunov Exponent fields. *IEEE Trans. Vis. Comput. Graph.* 18:1368–80

Beron-Vera FJ, Olascoaga MJ, Brown MG, Kocak H. 2012. Zonal jets as meridional transport barriers in the subtropical and polar lower stratosphere. *J. Atmos. Sci.* 69:753–67

Beron-Vera FJ, Olascoaga MJ, Brown MG, Kocak H, Rypina II. 2010. Invariant-tori-like Lagrangian coherent structures in geophysical flows. *Chaos* 20:017514

Beron-Vera FJ, Wang Y, Olascoaga MJ, Goni JG, Haller G. 2013. Objective detection of oceanic eddies and the Agulhas leakage. *J. Phys. Oceanogr.* 43:1426–38

Bettencourt JH, López C, Hernández-García E. 2013. Characterization of coherent structures in three-dimensional turbulent flows using the finite-size Lyapunov exponent. *J. Phys. A* 46:254022

Blazevski D, Haller G. 2014. Hyperbolic and elliptic transport barriers in three-dimensional unsteady flows. *Physica D* 273–274:46–64

Boffetta G, Lacorata G, Redaelli G, Vulpiani A. 2001. Detecting barriers to transport: a review of different techniques. *Physica D* 159:58–70

Bowman K. 2000. *Manifold geometry and mixing in observed atmospheric flows*. Unpublished manuscript, Texas A&M Univ.

Bozorgmagham AE, Ross SD, Schmale DG III. 2013. Real-time prediction of atmospheric Lagrangian coherent structures based on forecast data: an application and error analysis. *Physica D* 258:47–60

Branicki M, Wiggins S. 2009. An adaptive method for computing invariant manifolds in non-autonomous, three-dimensional dynamical systems. *Physica D* 238:1625–57

Branicki M, Wiggins S. 2010. Finite-time Lagrangian transport analysis: stable and unstable manifolds of hyperbolic trajectories and finite-time Lyapunov exponents. *Nonlinear Process. Geophys.* 17:1–36

Brunton SL, Rowley CW. 2010. Fast computation of finite-time Lyapunov exponent fields for unsteady flows. *Chaos* 20:017503

Budišić M, Mezić I. 2012. Geometry of the ergodic quotient reveals coherent structures in flows. *Physica D* 241:1255–69

Chelton DB, Schlax MG, Samelson RM. 2011. Global observations of nonlinear mesoscale eddies. *Prog. Oceanogr.* 91:167–216

Chian ACL, Rempel EL, Aulanier G, Schmieder B, Shadden SC, et al. 2014. Detection of coherent structures in turbulent photospheric flows. *Astrophys. J.* 786:51

Chong MS, Perry AE, Cantwell BJ. 1990. A general classification of three-dimensional flow fields. *Phys. Fluids A* 2:765–77

Claudel C-M, Virbhadra KS, Ellis GFR. 2001. The geometry of photon surfaces. *J. Math. Phys.* 42:818–38

Conti C, Rossinelli D, Koumoutsakos P. 2012. GPU and APU computations of finite-time Lyapunov exponent fields. *J. Comput. Phys.* 231:2229–44

Coulliette C, Lekien F, Paduan JD, Haller G, Marsden JE. 2007. Optimal pollution mitigation in Monterey Bay based on coastal radar data and nonlinear dynamics. *Environ. Sci. Technol.* 41:6562–72

Doerner R, Hubinger B, Martienssen W, Grossmann S, Thomae S. 1999. Stable manifolds and predictability of dynamical systems. *Chaos Solitons Fractals* 10:1759–82

d'Ovidio F, Fernández V, Hernández-García E, López C. 2004. Mixing structures in the Mediterranean Sea from finite size Lyapunov exponents. *Geophys. Res. Lett.* 31:L17203

Duc LH, Siegmund S. 2008. Hyperbolicity and invariant manifolds for planar nonautonomous systems on finite time intervals. *Int. J. Bifurc. Chaos Appl. Sci. Eng.* 3:641–74

Farazmand M, Blazevski D, Haller G. 2014. Shearless transport barriers in unsteady two-dimensional flows and maps. *Physica D* 278–279:44–57

Farazmand M, Haller G. 2012a. Computing Lagrangian coherent structures from variational LCS theory. *Chaos* 22:013128

Farazmand M, Haller G. 2012b. Erratum and addendum to "A variational theory of hyperbolic Lagrangian coherent structures" [Physica D 240 (2011) 574–598]. *Physica D* 241:439–41

Farazmand M, Haller G. 2013. Attracting and repelling Lagrangian coherent structures from a single computation. *Chaos* 15:023101

Farazmand M, Haller G. 2014. How coherent are the vortices of two-dimensional turbulence? *Phys. Fluids.* Submitted manuscript

Froyland G, Padberg-Gehle K. 2014. Almost-invariant and finite-time coherent sets: directionality, duration, and diffusion. In *Ergodic Theory, Open Dynamics, and Coherent Structures*, ed. W Bahsoun, C Bose, G Froyland, pp. 171–216. New York: Springer

Garth C, Gerhardt F, Tricoche X, Hagen H. 2007. Efficient computation and visualization of coherent structures in fluid flow applications. *IEEE Trans. Vis. Comput. Graph.* 13:1464–71

Green MA, Rowley CW, Haller G. 2007. Detection of Lagrangian coherent structures in three-dimensional turbulence. *J. Fluid Mech.* 572:111–20

Green MA, Rowley CW, Smits AJ. 2010. Using hyperbolic Lagrangian coherent structures to investigate vortices in bioinspired fluid flows. *Chaos* 20:017510

Green MA, Rowley CW, Smits AJ. 2011. The unsteady three-dimensional wake produced by a trapezoidal panel. *J. Fluid Mech.* 685:117–45

Guckenheimer J, Holmes P. 1983. *Nonlinear Oscillations, Dynamical Systems, and Bifurcations of Vector Fields*. New York: Springer

Gurtin ME. 1981. *An Introduction to Continuum Mechanics*. San Diego: Academic

Hadjighasem A, Haller G. 2014a. Detecting coherent structures from video streams of Jupiter. *Oberwolfach Rep.* In press

Hadjighasem A, Haller G. 2014b. Geodesic transport barriers in Jupiter's atmosphere: a video-based analysis. *SIAM Rev.* Submitted manuscript

Haller G. 2000. Finding finite-time invariant manifolds in two-dimensional velocity fields. *Chaos* 10:99–108

Haller G. 2001a. Distinguished material surfaces and coherent structures in three-dimensional fluid flows. *Physica D* 149:248–77

Haller G. 2001b. Lagrangian structures and the rate of strain in a partition of two-dimensional turbulence. *Phys. Fluids* 13:3365–85

Haller G. 2002. Lagrangian coherent structures from approximate velocity data. *Phys. Fluids* 14:1851–61

Haller G. 2005. An objective definition of a vortex. *J. Fluid Mech.* 525:1–26

Haller G. 2011. A variational theory of hyperbolic Lagrangian coherent structures. *Physica D* 240:574–98

Haller G, Beron-Vera FJ. 2012. Geodesic theory of transport barriers in two-dimensional flows. *Physica D* 241:1680–702

Haller G, Beron-Vera FJ. 2013. Coherent Lagrangian vortices: the black holes of turbulence. *J. Fluid Mech.* 731:R4

Haller G, Beron-Vera FJ. 2014. Addendum to "Coherent Lagrangian vortices: the black holes of turbulence." *J. Fluid Mech.* 755:R3

Haller G, Iacono R. 2003. Stretching, alignment, and shear in slowly varying velocity fields. *Phys. Rev. E* 68:056304

Haller G, Poje A. 1998. Finite time mixing in aperiodic flows. *Physica D* 119:352–80

Haller G, Sapsis T. 2011. Lagrangian coherent structures and the smallest finite-time Lyapunov exponent. *Chaos* 21:023115

Haller G, Yuan G. 2000. Lagrangian coherent structures and mixing in two-dimensional turbulence. *Physica D* 147:352–70

Haynes P, Shuckburgh E. 2000. Effective diffusivity as a diagnostic of atmospheric transport. 1. Stratosphere. *J. Geophys. Res.* 105:22777–94

Hua BL, Klein P. 1998. An exact criterion for the stirring properties of nearly two-dimensional turbulence. *Physica D* 113:98–110

Hua BL, McWilliams JC, Klein P. 1998. Lagrangian accelerations in geostrophic turbulence. *J. Fluid. Mech.* 366:87–108

Hunt JCR, Wray A, Moin P. 1988. *Eddies, stream, and convergence zones in turbulent flows*. Rep. CTR-S88, Cent. Turbul. Res., Stanford, CA

Ide K, Small D, Wiggins S. 2002. Distinguished hyperbolic trajectories in time-dependent fluid flows: analytical and computational approach for velocity fields defined as data sets. *Nonlinear Process. Geophys.* 9:237–63

Jeong J, Hussain F. 1995. On the identification of a vortex. *J. Fluid. Mech.* 285:69–94

Jones CKRT, Winkler S. 2002. Invariant manifolds and Lagrangian dynamics in the ocean and atmosphere. In *Handbook of Dynamical Systems*, Vol. 2, ed. B Fiedler, pp. 55–92. Amsterdam: Elsevier

Joseph B, Legras B. 2002. Relation between kinematic boundaries, stirring, and barriers for the Antarctic polar vortex. *J. Atmos. Sci.* 59:1198–212

Kafiabad HA, Chan PW, Haller G. 2013. Lagrangian detection of wind shear for landing aircraft. *J. Atmos. Ocean. Technol.* 30:2808–19

Karrasch D. 2012. Comment on "A variational theory of hyperbolic Lagrangian coherent structures [Physica D 240 (2011) 574–598]." *Physica D* 241:1470–73

Karrasch D. 2013. *Attracting Lagrangian coherent structures on Riemannian manifolds*. Unpublished manuscript, ETH Zürich, arXiv:1311.5043v3

Karrasch D, Haller G. 2013. Do Finite-Size Lyapunov Exponents detect coherent structures? *Chaos* 23:043126

Karrasch D, Huhn F, Haller G. 2014. Automated detection of coherent Lagrangian vortices in two-dimensional unsteady flows. *Proc. R. Soc. Lond. A.* Submitted manuscript

Kasten J, Petz C, Hotz I, Hege HC, Noack BR. 2010. Lagrangian feature extraction of the cylinder wake. *Phys. Fluids* 22:091108

Kelley DH, Allshouse MR, Ouellette NT. 2013. Lagrangian coherent structures separate dynamically distinct regions in fluid flow. *Phys. Rev. E* 88:013017

Kelley DH, Ouellette NT. 2011. Separating stretching from folding in fluid mixing. *Nat. Phys.* 7:477–80

LaCasce JH. 2008. Statistics from Lagrangian observations. *Prog. Oceanogr.* 77:1–29

Lai YC, Tél T. 2011. *Transient Chaos: Complex Dynamics on Finite Time Scales*. New York: Springer

Lapeyre G, Klein P, Hua BL. 1999. Does the tracer gradient vector align with the strain eigenvectors in 2-D turbulence? *Phys. Fluids* 11:3729–37

Lekien F, Ross SD. 2010. The computation of finite-time Lyapunov exponents on unstructured meshes and for non-Euclidean manifolds. *Chaos* 20:017505

Leung S. 2011. An Eulerian approach for computing the finite time Lyapunov exponent. *J. Comput. Phys.* 230:3500–24

Leung S. 2013. The backward phase flow method for the Eulerian finite time Lyapunov exponent computations. *Chaos* 23:043132

Lipinski D, Mohseni K. 2010. A ridge tracking algorithm and error estimate for efficient computation of Lagrangian coherent structures. *Chaos* 20:017504

Ma T, Bollt EM. 2014. Differential geometry perspective of shape coherence and curvature evolution by finite-time nonhyperbolic splitting. *SIAM J. Appl. Dyn. Syst.* 13:1106–36

Mahoney J, Bargteil D, Kingsbury M, Mitchell K, Solomon T. 2012. Invariant barriers to reactive front propagation in fluid flows. *Eur. Phys. Lett.* 98:44005

Mancho AM, Small D, Wiggins S, Ide K. 2003. Computation of stable and unstable manifolds of hyperbolic trajectories in two-dimensional, aperiodically time-dependent vector fields. *Physica D* 182:188–222

Mancho AM, Wiggins S, Curbelo J, Mendoza C. 2013. Lagrangian descriptors: a method for revealing phase space structures of general time dependent dynamical systems. *Commun. Nonlinear Sci. Numer. Simul.* 18:3530–57

Mathur M, Haller G, Peacock T, Ruppert-Felsot JE, Swinney HL. 2007. Uncovering the Lagrangian skeleton of turbulence. *Phys. Rev. Lett.* 98:144502

Mazloff MR, Heimbach P, Wunsch C. 2010. An eddy-permitting Southern Ocean state estimate. *J. Phys. Oceanogr.* 40:880–99

Mezić I. 2013. Analysis of fluid flows via spectral properties of the Koopman operator. *Annu. Rev. Fluid Mech.* 45:357–78

Mezić I, Loire S, Fonoberov V, Hogan P. 2010. A new mixing diagnostic and Gulf oil spill movement. *Science* 330:486–89

Mitchell KA, Mahoney JR. 2012. Invariant manifolds and the geometry of front propagation in fluid flows. *Chaos* 22:037104

Nakamura N. 1996. Two-dimensional mixing, edge formation, and permeability diagnosed in area coordinates. *J. Atmos. Sci.* 53:1524–37

Norgard G, Bremer P-T. 2012. Second derivative ridges are straight lines and the implications for computing Lagrangian coherent structures. *Physica D* 241:1475–76

Okubo A. 1970. Horizontal dispersion of floatable particles in the vicinity of velocity singularities such as convergences. *Deep-Sea Res.* 17:445–54

Olascoaga MJ, Beron-Vera FJ, Haller G, Trinanes J, Iskandarani M, et al. 2013. Drifter motion in the Gulf of Mexico constrained by altimetric Lagrangian coherent structures. *Geophys. Res. Lett.* 40:6171–75

Olascoaga MJ, Haller G. 2012. Forecasting sudden changes in environmental pollution patterns. *Proc. Natl. Acad. Sci. USA* 109:4738–43

Onu K, Huhn F, Haller G. 2014. LCS Tool: an algorithmic introduction to Lagrangian coherent structures. *J. Comput. Sci.* Submitted manuscript

Ottino JM. 1989. *The Kinematics of Mixing: Stretching, Chaos, and Transport*. Cambridge, UK: Cambridge Univ. Press

Ouellette NT. 2012. On the dynamical role of coherent structures in turbulence. *C. R. Phys.* 13:866–77

Palmerius KL, Cooper M, Ynnerman A. 2009. Flow field visualization using vector field perpendicular surfaces. *Proc. 25th Spring Conf. Comput. Graph.*, pp. 27–34. New York: ACM

Peacock T, Dabiri J, eds. 2010. Focus issue on Lagrangian coherent structures. *Chaos* (*Special Issue*) Vol. 20(1). Melville, NY: AIP

Peacock T, Haller G. 2013. Lagrangian coherent structures: the hidden skeleton of fluid flows. *Phys. Today* 66:41–47

Peikert R, Pobitzer A, Sadlo F, Schindler B. 2014. A comparison of finite-time and finite-size Lyapunov exponents. In *Topological Methods in Data Analysis and Visualization III*, ed. P-T Bremer, I Hotz, V Pascucci, R Peikert, pp. 187–200. Berlin: Springer

Peng J, Dabiri JO. 2009. Transport of inertial particles by Lagrangian coherent structures: application to predator-prey interaction in jellyfish feeding. *J. Fluid Mech.* 623:75–84

Pierrehumbert RT, Yang H. 1993. Global chaotic mixing on isentropic surfaces. *J. Atmos. Sci.* 50:2462–80

Provenzale A. 1999. Transport by coherent barotropic vortices. *Annu. Rev. Fluid Mech.* 31:55–93

Raben SG, Ross SD, Vlachos PV. 2014a. Computation of finite-time Lyapunov exponents from time-resolved particle image velocimetry data. *Exp. Fluids* 55:1638

Raben SG, Ross SD, Vlachos PV. 2014b. Demonstration of experimental three-dimensional finite-time Lyapunov exponents with inertial particles. *Phys. Rev. E.* Submitted manuscript

Rempel EL, Chian ACL, Brandenburg A, Muñoz PR, Shadden SC. 2013. Coherent structures and the saturation of a nonlinear dynamo. *J. Fluid Mech.* 729:309–29

Sadlo F, Peikert R. 2007. Efficient visualization of Lagrangian coherent structures by filtered AMR ridge extraction. *IEEE Trans. Vis. Comput. Graph.* 13:1456–63

Sadlo F, Rigazzi A, Peikert R. 2010. Time-dependent visualization of Lagrangian coherent structures by grid advection. In *Topological Methods in Data Analysis and Visualization*, ed. V Pascucci, X Tricoche, H Hagen, J Tierny, pp. 151–65. Berlin: Springer

Samelson RM. 2013. Lagrangian motion, coherent structures, and lines of persistent material strain. *Annu. Rev. Marine Sci.* 5:137–63

Samelson RM, Wiggins S. 2006. *Lagrangian Transport in Geophysical Jets and Waves*. New York: Springer

Sapsis T, Peng J, Haller G. 2011. Instabilities of prey dynamics in jellyfish feeding. *Bull. Math. Biol.* 73:1841–56

Schindler B, Peikert R, Fuchs R, Theisel H. 2012. Ridge concepts for the visualization of Lagrangian coherent structures. In *Topological Methods in Data Analysis and Visualization II*, ed. R Peikert, H Hauser, H Carr, R Fuchs, pp. 221–36. Berlin: Springer

Shadden SC. 2012. Lagrangian coherent structures. In *Transport and Mixing in Laminar Flows: From Microfluidics to Oceanic Currents*, ed. R Grigoriev, pp. 59–89. Berlin: Wiley-VCH

Shadden SC, Lekien F, Marsden JE. 2005. Definition and properties of Lagrangian coherent structures from finite-time Lyapunov exponents in two-dimensional aperiodic flows. *Physica D* 212:271–304

Shadden SC, Lekien F, Marsden JE. 2007. Lagrangian coherent structures in *n*-dimensional systems. *J. Math. Phys.* 48:065404

Shuckburgh E. 2012. Mapping unstable manifolds using drifters/floats in a Southern Ocean field campaign. *AIP Conf. Proc.* 1479:650–53

Shuckburgh E, Haynes P. 2003. Diagnosing transport and mixing using a tracer-based coordinate system. *Phys. Fluids* 15:3342–57

Sulman MHM, Huntley HS, Lipphardt BL, Kirwan AD. 2013. Leaving flatland: diagnostics for Lagrangian coherent structures in three-dimensional flows. *Physica D* 258:77–92

Tabor M, Klapper I. 1994. Stretching and alignment in chaotic and turbulent flows. *Chaos Solitons Fractals* 4:1031–55

Tang W, Chan PW, Haller G. 2010a. Accurate extraction of LCS over finite domains, with application to flight safety analysis over Hong Kong International Airport. *Chaos* 20:017502

Tang W, Chan PW, Haller G. 2011a. Lagrangian coherent structure analysis of terminal winds detected by LIDAR. Part I: turbulence structures. *J. Appl. Meteorol. Climatol.* 50:325–33

Tang W, Chan PW, Haller G. 2011b. Lagrangian coherent structure analysis of terminal winds detected by LIDAR. Part II: Structure evolution and comparison with flight data. *J. Appl. Meteorol. Climatol.* 50:325–38

Tang W, Mathur M, Haller G, Hahn DC, Ruggiero FH. 2010b. Lagrangian coherent structures near a subtropical jet stream. *J. Atmos. Sci.* 67:2307–19

Teramoto H, Haller G, Komatsuzaki T. 2013. Detecting invariant manifolds as stationary LCSs in autonomous dynamical systems. *Chaos* 23:043107

Truesdell C, Noll W. 2004. *The Non-Linear Field Theories of Mechanics*. New York: Springer

von Hardenberg J, Fraedrich K, Lunkeit F, Provenzale A. 2000. Transient chaotic mixing during a baroclinic life cycle. *Chaos* 10:122–34

Voth GA, Haller G, Gollub JP. 2002. Experimental measurements of stretching fields in fluid mixing. *Phys. Rev. Lett.* 88:254501

Weiss J. 1991. The dynamics of enstrophy transfer in two-dimensional hydrodynamics. *Physica D* 48:273–94

Wiggins S. 1992. *Chaotic Transport in Dynamical Systems*. New York: Springer

Wiggins S. 2005. The dynamical systems approach to Lagrangian transport in oceanic flows. *Annu. Rev. Fluid Mech.* 37:295–328

Yeates AR, Hornig G, Welsch BT. 2012. Lagrangian coherent structures in photospheric flows and their implications for coronal magnetic structure. *Astron. Astrophys.* 539:A1

Contents

Indexes

Errata

An online log of corrections to *Annual Review of Fluid Mechanics* articles may be found
at http://www.annualreviews.org/errata/fluid